

Studies of granularity of a hadronic calorimeter for tens-of-TeV jets at a 100 TeV pp collider

C.-H. Yeh^a, S.V. Chekanov^b, A.V. Kotwal^{c,d}, J. Proudfoot^b, S. Sen^c, N.V. Tran^d, S.-S. Yu^a

^a *Department of Physics, National Central University, Chung-Li, Taoyuan City 32001, Taiwan*

^b *HEP Division, Argonne National Laboratory, 9700 S. Cass Avenue, Argonne, IL 60439, USA.*

^c *Department of Physics, Duke University, USA*

^d *Fermi National Accelerator Laboratory*

^e *Department of Physics, Michigan State University, 220 Trowbridge Road, East Lansing, MI 48824*

Abstract

Jet substructure variables for hadronic jets with transverse momenta in the range from 2.5 TeV to 20 TeV were studied using several designs for spacial size of calorimeter cells. The studies used the full Geant4 simulation of calorimeter response combined with realistic reconstruction of calorimeter clusters. In most cases considered in this study the results indicate that the performance of jet-substructure reconstruction improves with reducing cell sizes of a hadronic calorimeter from $\Delta\eta \times \Delta\phi = 0.087 \times 0.087$ to 0.022×0.022 .

Keywords: multi-TeV physics, pp collider, future hadron colliders, FCC, SppC

1. Introduction

Particle collisions at energies beyond those attained at the LHC will lead to many challenges for detector technologies. Future experiments, such as high-energy LHC (HE-LHC), future circular pp colliders of the European initiative, FCC-hh [1] and the Chinese initiative, SppC [2] will be required to measure high-momentum bosons (W , Z , H) and top quarks with strongly collimated decay products that form jets. Jet substructure techniques are used to identify such highly boosted particles, and thus can maximize the physics potential of the future colliders.

The reconstruction of jet substructure variables for collimated jets with transverse momentum above 10 TeV requires an appropriate detector design. The most important for reconstruction of such jets are tracking and calorimetry. Recently, a number of studies [3, 4, 5] have been discussed using various fast simulation tools, such as Delphes [6], in which momenta of particles are smeared to mimic detector response.

A major step towards the usage of full Geant4 simulation to verify the granularity requirements for calorimeters was made in [7]. These studies have illustrated

Email addresses: jwuzelski18@gmail.com (C.-H. Yeh), chekanov@anl.gov (S.V. Chekanov), ashutosh.kotwal@duke.edu (A.V. Kotwal), proudfoot@anl.gov (J. Proudfoot), sourav.sen@duke.edu (S. Sen), ntran@fnal.gov (N.V. Tran), syu@cern.ch (S.-S. Yu)

16 a significant impact of granularity of electromagnetic (ECAL) and hadronic (HCAL)
 17 calorimeters on the shape of hadronic showers calculated using calorimeter hits for two
 18 particles separated by some angle. It was concluded that high granularity is essential
 19 in resolving two close-by particles for energies above 100 GeV.

20 This paper makes another step in understanding of this problem in terms of high-
 21 level physics quantities typically used in physics analyses. Similar to the studies pre-
 22 sented in [7], this paper is based on a full Geant4 simulation with realistic jet recon-
 23 struction.

24 2. Simulation of detector response

25 The description of the detector and software used for this study is discussed in [7].
 26 We use the SiFCC detector geometry with a software package that represents a versatile
 27 environment for simulations of detector performance, testing new technology options,
 28 and event reconstruction techniques for future 100 TeV colliders.

29 The baseline detector discussed in [7] uses a steel-scintillator hadronic calorimeter
 30 with a transverse cell size of $5 \times 5 \text{ cm}^2$, which corresponds to $\Delta\eta \times \Delta\phi = 0.022 \times 0.022$,
 31 where η is the pseudorapidity, $\eta \equiv -\ln \tan(\theta/2)$, and ϕ is the azimuthal angle. The
 32 depth of the HCAL in the barrel region is about 11.25 interaction lengths (λ_I). The
 33 HCAL has 64 longitudinal layers in the barrel and the endcap regions.

34 In addition, to the baseline HCAL geometry, several geometry variations were con-
 35 sidered. We used the HCAL with the cells that have the transverse size of $20 \times 20 \text{ cm}^2$,
 36 $2 \times 2 \text{ cm}^2$ and $1 \times 1 \text{ cm}^2$. In the terms of $\Delta\eta \times \Delta\phi$, such cell sizes correspond to
 37 0.087×0.087 , 0.0087×0.0087 and 0.0043×0.0043 , respectively.

38 The GEANT4 (version 10.3) [8] simulation of calorimeter response was complemented
 39 with the full reconstruction of calorimeter clusters formed by the Pandora algorithm
 40 [9, 10]. Calorimeter clusters were built from calorimeter hits in the ECAL and HCAL
 41 after applying the corresponding sampling fractions. No other corrections are applied.
 42 Hadronic jets were reconstructed with the FASTJET package [11] using the anti- k_T
 43 algorithm [12] with a distance parameter of 0.5.

44 In the following discussion, we use the simulations of a heavy Z' boson, a hypo-
 45 thetical gauge boson that arises from extensions of the electroweak symmetry of the
 46 Standard Model. The Z' bosons were simulated with the masses $M = 5, 10, 20$ and
 47 40 TeV. The lowest value represents a typical mass that is within the reach of the LHC
 48 experiments. The value 40 TeV represents the physics reach for a 100 TeV collider. The
 49 Z' particles are forced to decay to two light-flavor jets ($q\bar{q}$), W^+W^- or $t\bar{t}$, where W and
 50 t decay hadronically. In all such scenarios, two highly boosted jets are produced, which
 51 are typically back-to-back in the laboratory frame. The typical transverse momenta
 52 of such jets are $\simeq M/2$. The main difference between considered decay types lays in
 53 different jet substructure. In the case of the $q\bar{q}$ decays, jets do not have any internal
 54 structure. In the case of W^+W^- , each jet originates from W , thus it has two subjets
 55 because of the decay $W \rightarrow q\bar{q}$. In the case of hadronic top decays, jets have three
 56 subjets due to the decay $t \rightarrow W^+ b \rightarrow q\bar{q}b$. The signal events were generated using the
 57 PYTHIA8 generator with the default settings, ignoring interference with SM processes.
 58 The event samples used in this paper are available from the HepSim database [13].

59 3. Studies of jet properties

60 We consider several variables that represent jet substructure using different types of
 61 calorimeter granularity. The question we want to answer is how close the reconstructed
 62 jet substructure variables reflect the input “truth” values that are reconstructed using
 63 input particles directly from the PYTHIA8 generator.

64 In this study we use the jet effective radius and jet splitting scales as benchmark
 65 variables to study jet substructure properties for different calorimeter granularity sce-
 66 narios. The effective radius is the average of the energy weighted radial distance δR_i in
 67 $\eta - \phi$ space of jet constituents. It is defined as $(1/E) \sum_i e_i \delta R_i$, where E is the energy
 68 of the jet and e_i is the energy of a calorimeter cluster i at the distance δR_i from the jet
 69 center. The sum runs over all constituents of the jet. Recently, it has been studied for
 70 multi-TeV jets in Ref.[14]. A jet k_T splitting scale [15] is defined as a distance measure
 71 used to form jets by the k_T recombination algorithm [16, 17]. This variable has been
 72 studied by ATLAS [18], and more recently in the context of 100 TeV physics [14]. The
 73 splitting scale is defined as $\sqrt{d_{12}} = \min(p_T^1, p_T^2) \times \delta R_{12}$ [18] at the final stage of the k_T
 74 clustering, where two subjects are merged into the final one.

75 Figures 1 and 2 show the distributions of the jet effective radius and jet splitting
 76 scale for different jet transverse momenta and HCAL granularities. The reconstructed-
 77 level distributions significantly disagree with the distributions reconstructed using truth-
 78 level particles. The distribution reconstructed with the cell sizes $1 \times 1 \text{ cm}^2$ are clos-
 79 est to the truth-level variables. The distributions reconstructed using the cell size of
 80 $20 \times 20 \text{ cm}^2$, show the largest discrepancy with the truth-level variables. Note that, in
 81 terms of closeness of reconstructed distributions to the truth level, there is no significant
 82 difference between $5 \times 5 \text{ cm}^2$, $2 \times 2 \text{ cm}^2$ and $1 \times 1 \text{ cm}^2$ choices.

83 Thus this study confirms the baseline SiFCC detector geometry [7] that uses $5 \times$
 84 5 cm^2 cells, corresponding to $\Delta\eta \times \Delta\phi = 0.022 \times 0.022$. Note that the ATLAS and CMS
 85 detectors use the HCAL cell sizes in the barrel region which are close to $\Delta\eta \times \Delta\phi =$
 86 0.087×0.087 . According to this study, such HCAL cell sizes are not optimal in terms
 87 of performance for tens-of-TeV jets.

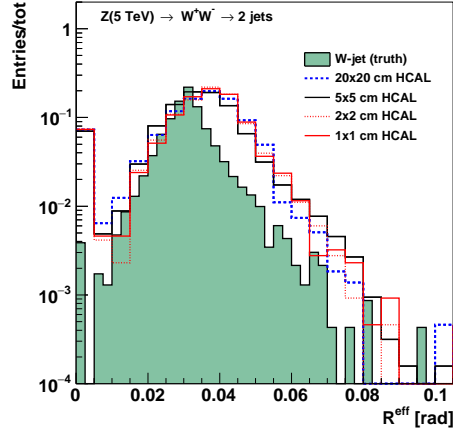
88 In the next few sections we will consider several other physics-motivated variables
 89 that can shed light upon the performance of the HCAL for tens-of-TeV jets.

90 4. Study of detector performance with soft drop mass

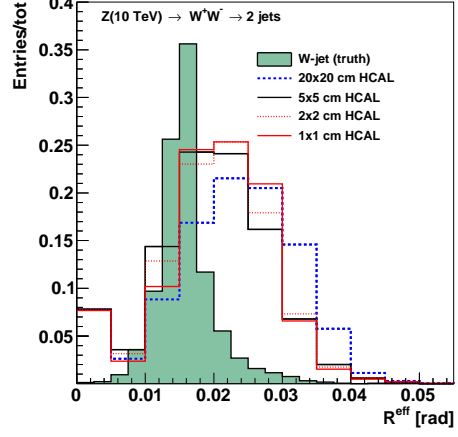
91 In this section, we use the jet mass computed with a specific algorithm, soft drop
 92 declustering, to study the performance of detector with various detector cell sizes and
 93 center-of-mass (c.m.) energies.

94 4.1. The technique of soft drop declustering

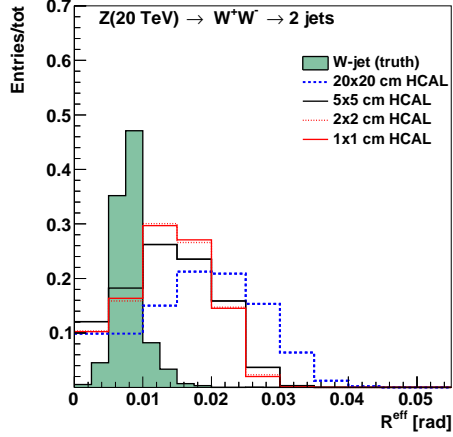
95 The soft drop declustering [19] is a grooming method that removes soft wide-
 96 angle radiation from a jet. The constituents of a jet j_0 are first reclustered using
 97 the Cambridge-Aachen (C/A) algorithm [20, 21]. Then, the jet j_0 is broken into two
 98 subjects j_1 and j_2 by undoing the last stage of C/A clustering. If the subjects pass
 99 the following soft drop condition, jet j_0 is the final soft-drop jet. Otherwise, the algo-
 100 rithm redefines j_0 to be the subject with larger p_T (among j_1 and j_2) and iterates the



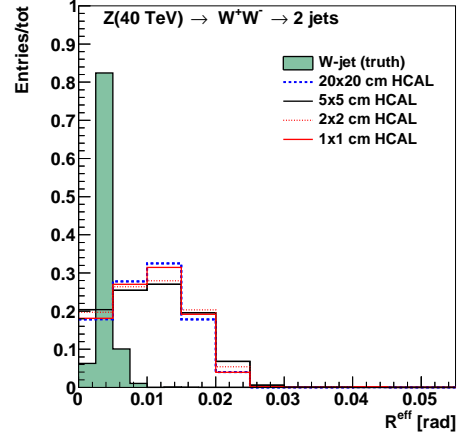
(a) 5 TeV



(b) 10 TeV

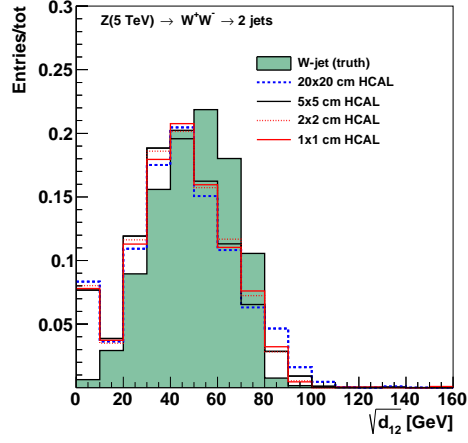


(c) 20 TeV

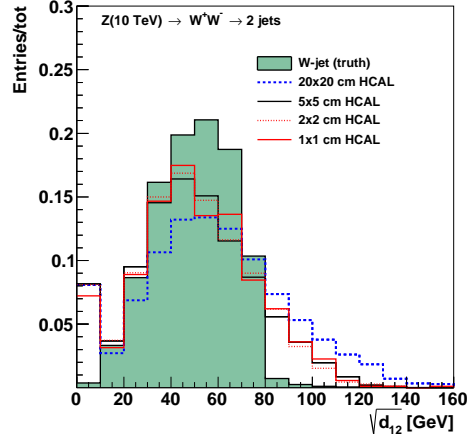


(d) 40 TeV

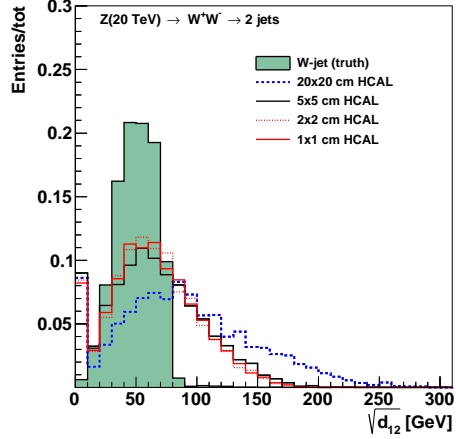
Figure 1: Jet effective radius for different jet transverse momenta and HCAL granularities.



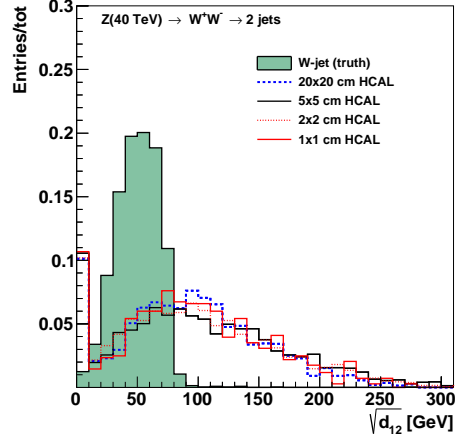
(a) 5 TeV



(b) 10 TeV



(c) 20 TeV



(d) 40 TeV

Figure 2: Jet splitting scale for different jet transverse momenta and HCAL granularity.

101 procedure.

$$\frac{\min(p_{T1}, p_{T2})}{p_{T1} + p_{T2}} > z_{\text{cut}} \left(\frac{\Delta R_{12}}{R_0} \right)^\beta, \quad (1)$$

102 where p_{T1} and p_{T2} are the transverse momenta of the two subjets, z_{cut} is soft drop
 103 threshold, ΔR_{12} is the distance between the two subjets in the rapidity-azimuth angle
 104 plane (y - ϕ), R_0 is the characteristic radius of the original jet, and β is the angular
 105 exponent.

106 In our study, we compare the performance of a future detector when setting $\beta = 0$
 107 versus when setting $\beta = 2$. For $\beta = 0$, the soft drop condition depends only on the z_{cut} .
 108 For $\beta = 2$, the condition depends on the angular distance between the two subjets and
 109 z_{cut} and the algorithm becomes infrared and collinear safe.

110 4.2. Analysis method

111 We employ the following method to quantify the detector performance and de-
 112 termine the cell size that gives the best separation power to distinguish signal from
 113 background. For each configuration of detector and c.m. energy, we draw the receiver
 114 operating characteristic (ROC) curves in which the x-axis is the signal efficiency (ϵ_{sig})
 115 and y-axis is the inverse of background efficiency ($1/\epsilon_{\text{bkg}}$). In order to scan the efficien-
 116 cies of soft drop mass cuts, we vary the mass window as follows. We first look for the
 117 median bin i_{med}^1 of the soft drop mass histogram from simulated signal events. Taking
 118 the right boundary of bin i_{med} as the center of mass window x_{center} , we start increasing
 119 the width of mass window symmetrically on the left and on the right of x_{center} , in steps
 120 of 5 GeV, i.e. the narrowest mass window is $[x_{\text{center}} - 5, x_{\text{center}} + 5]$. If one side reaches
 121 the boundary of the mass histogram, we only increase the width on the other side, also
 122 in steps of 5 GeV. For each mass window, there will be corresponding ϵ_{sig} and ϵ_{bkg} ,
 123 which gives a point in the ROC curves.

124 4.3. Results and conclusion

125 Figures 3, 5, 7, and 9 show a few representative distributions for the soft drop mass
 126 for $\beta = 0$ and $\beta = 2$ with different c.m. energies and detector cell sizes; the signals
 127 considered are $Z' \rightarrow WW$ and $Z' \rightarrow t\bar{t}$. Figures 4, 6, 8, and 10 show the ROC curves
 128 for different detector cell sizes and c.m. energies.

129 These studies show that the reconstruction of soft drop mass improves with decrease
 130 of the HCAL cell sizes. Figures 4 and 6 show that for $\beta = 0$ the smallest detector cell
 131 size, 1 cm \times 1 cm, has the best separation power at $\sqrt{s} = 5, 10$, and 20 TeV when the
 132 signal is $Z' \rightarrow WW$, and at $\sqrt{s} = 10$ and 20 TeV when the signal is $Z' \rightarrow t\bar{t}$. On the
 133 contrary, Figs. 8 and 10 show that for $\beta = 2$ the smallest detector cell size does not
 134 have improvements in the separation power with respect to those with larger cell sizes.
 135 In fact, the performances of the three cell sizes are similar. In addition, sometimes
 136 bigger detector cell sizes, 5 cm \times 5 cm or 20 cm \times 20 cm have the best separation power.

137 We also find that the soft drop mass with $\beta = 0$ has better performance for distin-
 138 guishing signal from background than for $\beta = 2$. Therefore, we will apply requirements
 139 on this variable when studying the other jet substructure variables.

¹The integral from bin 0 to bin i_{med} ($i_{\text{med}} - 1$) should be greater (less) than half of the total number of events. Note, the bin width is 5 GeV.

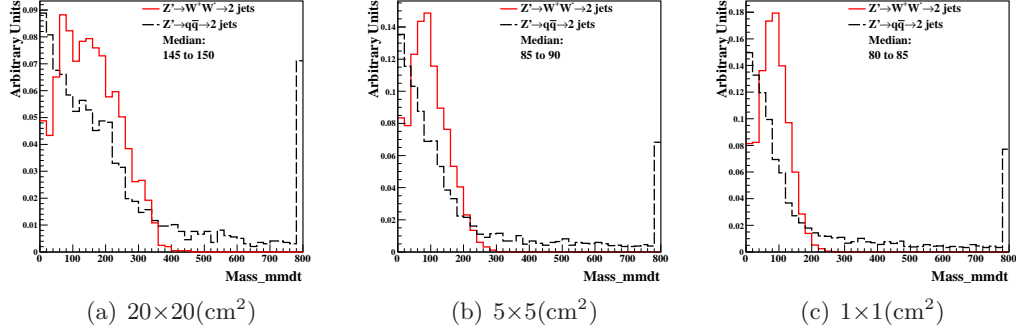


Figure 3: Distributions of soft drop mass for $\beta=0$, with 20 TeV c.m. energies and three different detector cell sizes: 20×20 , 5×5 , and 1×1 (cm^2). The signal (background) process is $Z' \rightarrow WW$ ($Z' \rightarrow q\bar{q}$).

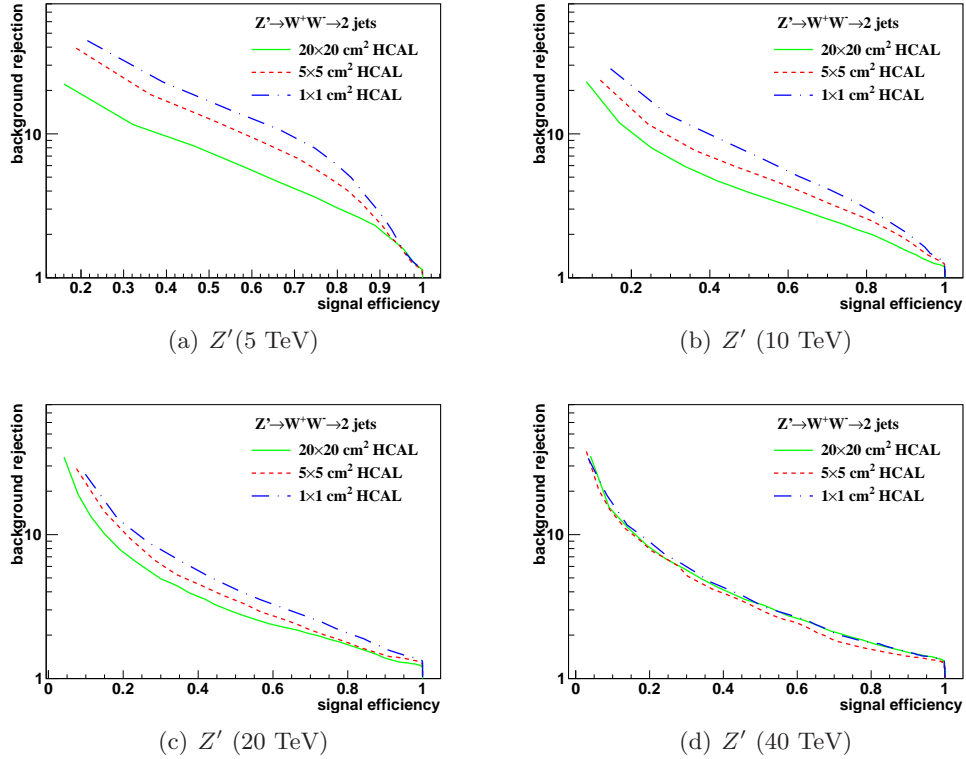


Figure 4: The ROC curves of soft drop mass selection for $\beta=0$ with 5, 10, 20, 40 TeV c.m. energies. Three different detector cell sizes are compared: 20×20 , 5×5 , and 1×1 (cm^2). The signal (background) process is $Z' \rightarrow WW$ ($Z' \rightarrow q\bar{q}$).

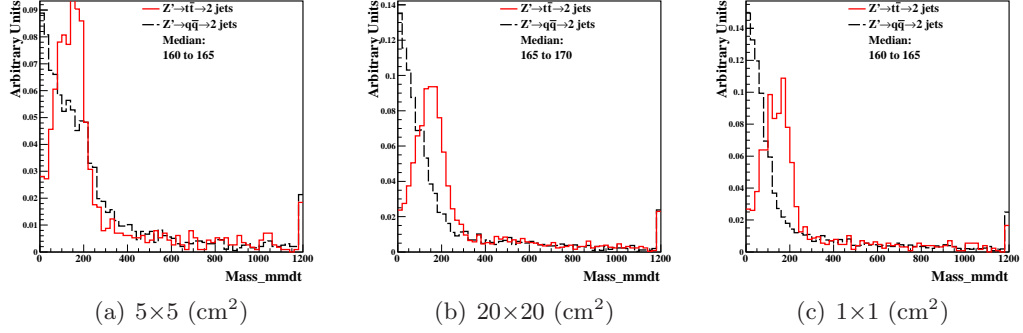


Figure 5: Distributions of soft drop mass for $\beta=0$, with 20 TeV c.m. energies and three different detector cell sizes: 20×20 , 5×5 , and 1×1 (cm^2). The signal (background) process is $Z' \rightarrow t\bar{t}$ ($Z' \rightarrow q\bar{q}$).

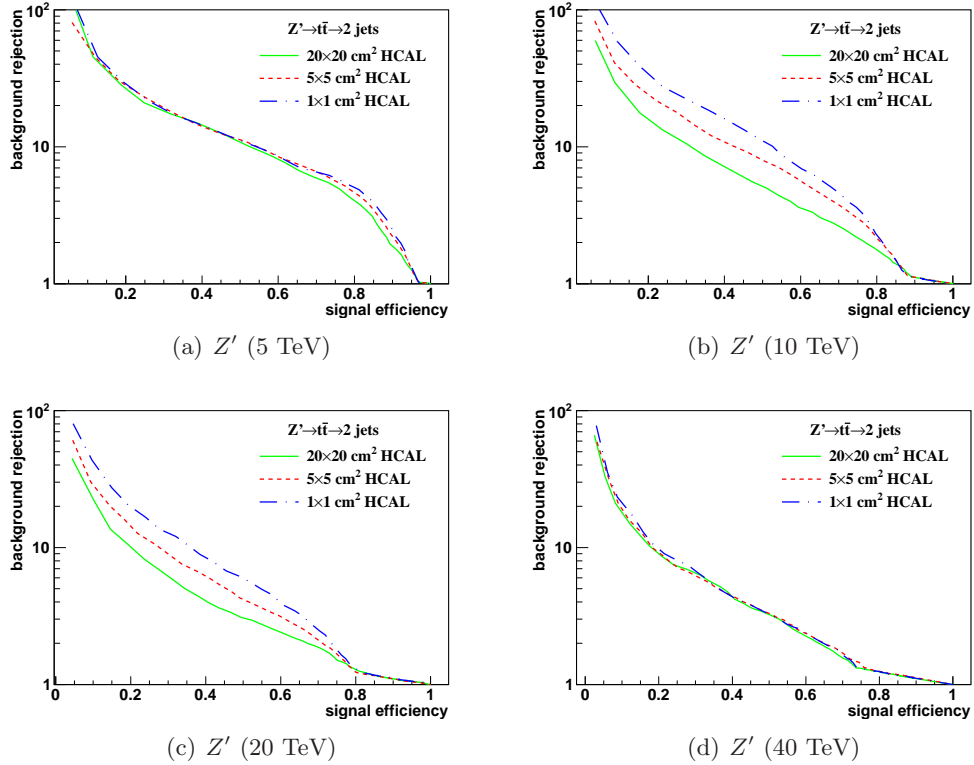


Figure 6: The ROC curves of soft drop mass selection for $\beta=0$ with 5, 10, 20, 40 TeV c.m. energies. Three different detector cell sizes are compared: 20×20 , 5×5 , and 1×1 (cm^2). The signal (background) process is $Z' \rightarrow t\bar{t}$ ($Z' \rightarrow q\bar{q}$).

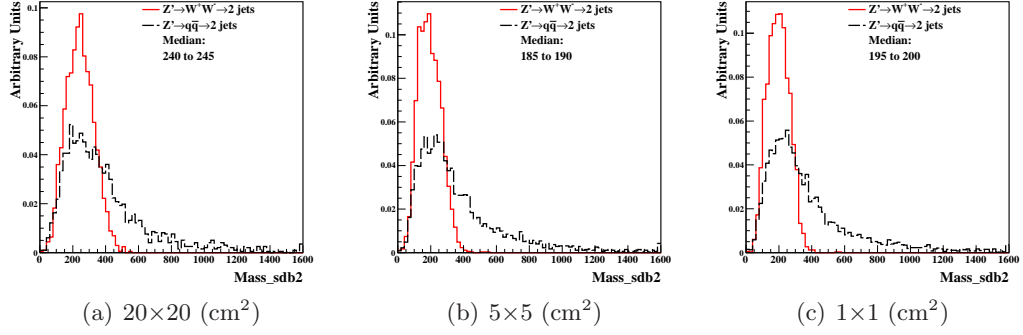


Figure 7: Distributions of soft drop mass for $\beta=2$, with 20 TeV c.m. energies and three different detector cell sizes: 20×20 , 5×5 , and 1×1 (cm^2). The signal (background) process is $Z' \rightarrow WW$ ($Z' \rightarrow q\bar{q}$).

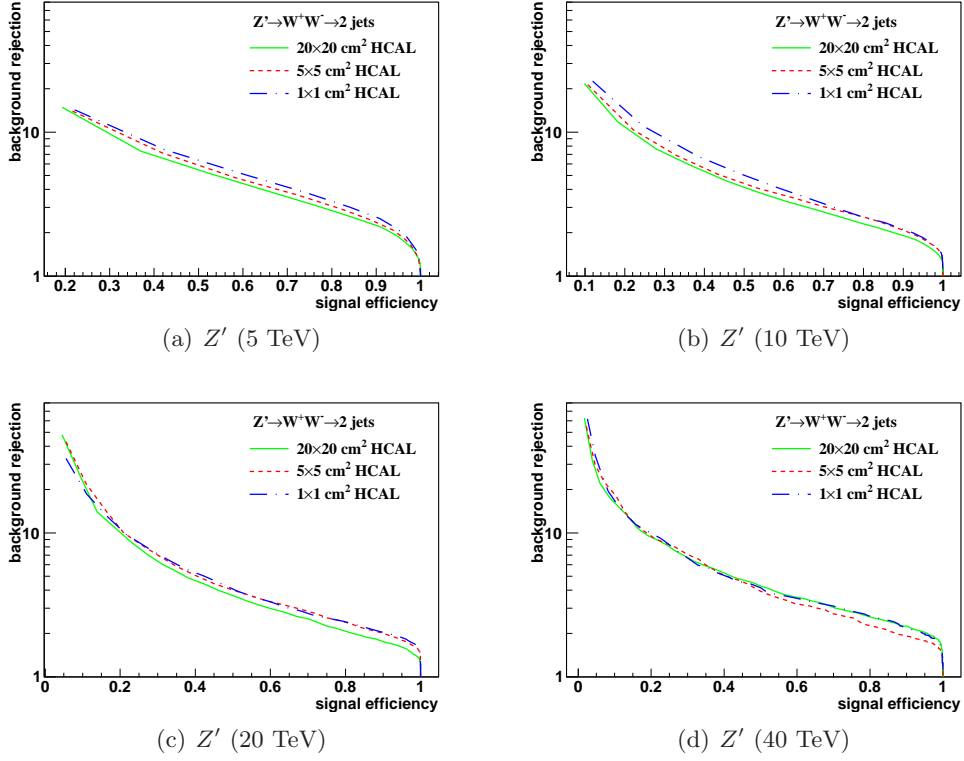


Figure 8: The ROC curves of soft drop mass selection for $\beta=2$ with 5, 10, 20, 40 TeV c.m. energies. Three different detector cell sizes are compared: 20×20 , 5×5 , and 1×1 (cm^2). The signal (background) process is $Z' \rightarrow WW$ ($Z' \rightarrow q\bar{q}$).

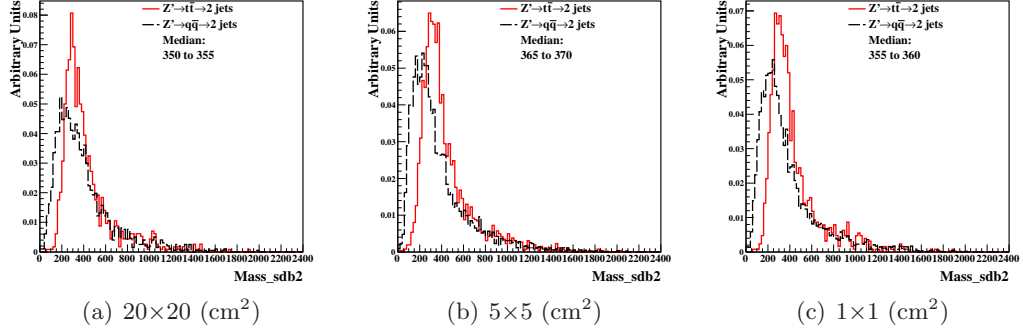


Figure 9: Distributions of soft drop mass for $\beta=2$, with 20 TeV c.m. energies and three different detector cell sizes: 20×20 , 5×5 , and 1×1 (cm^2). The signal (background) process is $Z' \rightarrow t\bar{t}$ ($Z' \rightarrow q\bar{q}$).

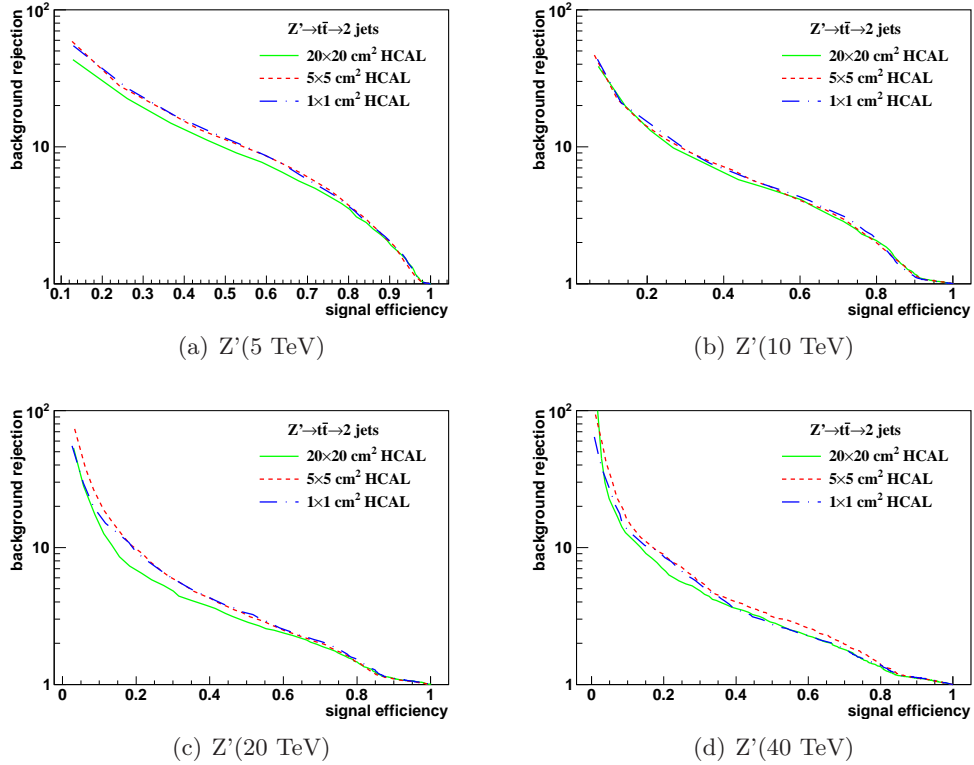


Figure 10: The ROC curves of soft drop mass selection for $\beta=2$ with 5, 10, 20, 40 TeV c.m. energies. Three different detector cell sizes are compared: 20×20 , 5×5 , and 1×1 (cm^2). The signal (background) process is $Z' \rightarrow t\bar{t}$ ($Z' \rightarrow q\bar{q}$).

140 5. Study of detector performance with jet substructure variables

141 In this section, we use several jet substructure variables to study the performance
142 of detector with various detector cell sizes and c.m. energies.

143 5.1. N -subjettiness

144 The variable N -subjettiness [22], denoted by τ_N , is designed to “count” the number
145 of subjet(s) in a large radius jet so to separate signal jets from decays of heavy bosons
146 and background jets from QCD processes. The τ_N is the p_T -weighted angular distance
147 between each jet constituent and the closest subjet axis:

$$\tau_N = \frac{1}{d_0} \sum_k p_{T,k} \min\{\Delta R_{1,k}, \Delta R_{2,k}, \dots, \Delta R_{N,k}\}, \quad (2)$$

148 with a normalization factor d_0 :

$$d_0 = \sum_k p_{T,k} R_0.$$

149 The k runs over all constituent particles in a given large radius jet, $p_{T,k}$ is the transverse
150 momentum of each individual constituent particle, $\Delta R_{j,k} = \sqrt{(\Delta y)^2 + (\Delta \phi)^2}$ is the
151 distance between the constituent particle k and the candidate subjet axis j in the $y - \phi$
152 plane. The R_0 is the characteristic jet radius used in the anti- k_t jet algorithm.

153 This analysis uses the jet reconstruction described in Sect. 2. The subjet axes are
154 obtained by running the exclusive k_t algorithm [23] and reversing the last N clustering
155 steps. Namely, when τ_N is computed, the k_t algorithm is forced to return exactly N
156 jets. If a large radius jet has N subjet(s), its τ_N is smaller than τ_{N-1} . Therefore, in our
157 analysis, the ratio of the τ_N variables, τ_{21} (τ_2/τ_1) and τ_{32} (τ_3/τ_2), are used to distinguish
158 the one-prong background jets and the two-prong jets from W or the three-prong jets
159 from top.

160 We use the ROC curves as described in Section 4.2 to analyze the detector perfor-
161 mance and determine the cell size that gives the best separation power to distinguish
162 signal from background. Following the suggestion by Ref. [24], the requirement on the
163 soft drop mass with $\beta = 0$ is applied before the study of N -subjettiness. For each
164 detector configuration and c.m. energy, the soft drop mass selection is determined as
165 follows. First, we look for the median bin of the soft drop mass histogram from sim-
166 ulated signal events as described in Section 4.2. Then, we compare the numbers of
167 events in the bins adjacent to the medium bin (bin $i_{\text{med}} - 1$ and bin $i_{\text{med}} + 1$). The bin
168 with larger number of events is added, in addition to the medium bin, to extend the
169 mass window. The procedure is repeated until the window contains at least 75% of the
170 total number of signal events.

171 In order to obtain the signal and background efficiencies, various ranges of τ_{21} and
172 τ_{32} are scanned. Since some of the background distributions have long tails and leak into
173 the signal-dominated region, we use the following method as suggested by the Pearson
174 Lemma Method to determine the ranges of τ variables. First, we take the ratio of
175 the signal to background τ_{21} (τ_{32}) histograms. The boundaries of the bin (seed bin)
176 with maximum signal to background ratio (S/N) give us the first range of τ selection:

177 $x_{\text{low}}^{\text{seedbin}} < \tau_{21} < x_{\text{high}}^{\text{seedbin}}$. Then, we compare the S/N in the bins adjacent to the seed
 178 bin. The bin with larger S/N is added, in addition to the seed bin, to extend the τ_{21}
 179 selection window. Every window has its corresponding ϵ_{sig} and $1/\epsilon_{\text{bkg}}$ and an ROC
 180 curve is mapped out.

181 In addition to the ROC curves, we use the so-called "Mann-Whitney" test to quan-
 182 tify the detector performance. The value of Mann-Whitney is related to the integrated
 183 area under the ROC curve: if the value is bigger, it indicates the signal and background
 184 distributions have similar shapes and can not be well separated from each other. Vice
 185 versa, if the value is smaller, we can achieve a better signal and background separation.

186 Figures 11 and 13 show the distributions of τ_{21} and τ_{32} for $\sqrt{s} = 20$ TeV after
 187 applying the requirement on the soft drop mass. The signals considered are $Z' \rightarrow WW$
 188 (τ_{21}) and $Z' \rightarrow t\bar{t}$ (τ_{32}). Figures 12 and 14 present the ROC curves from different
 189 detector cell sizes and c.m. energies, respectively. The smallest detector cell size
 190 ($1 \times 1 \text{ cm}^2$) does not have the best separation power. In fact, in some cases, the
 191 best separation power comes from a detector with bigger cell sizes ($5 \times 5 \text{ cm}^2$ and
 192 $20 \times 20 \text{ cm}^2$).

193 Figures 17 (a) and (b) present the summary plots of τ_{21} and τ_{32} with various detector
 194 cell sizes and c.m. energies using Mann Whitney U test. For τ_{21} at smaller c.m.
 195 energies, when the cell size is smaller, the detector performance improves. However,
 196 when c.m. energy increases, no improvement is observed using the smallest detector
 197 cell size ($1 \times 1 \text{ cm}^2$). For τ_{32} , the case is similar to τ_{21} . It is interesting to note that at
 198 very large c.m. energies, the large detector cell sizes ($5 \times 5 \text{ cm}^2$ and $20 \times 20 \text{ cm}^2$) have
 199 a better separation power than the smallest cell size considered in this analysis.

200 5.2. Energy correlation function

201 The energy correlation function (ECF) [25] is defined as follows:

$$ECF(N, \beta) = \sum_{i_1 < i_2 < \dots < i_N \in J} \left(\prod_{a=1}^N p_{Tia} \right) \left(\prod_{b=1}^{N-1} \prod_{c=b+1}^N R_{i_b i_c} \right)^\beta, \quad (3)$$

202 where the sum is looped all particles in the jet J , p_T is the transverse momentum of
 203 each individual particle, and R is the distance between two particles in the y - ϕ plane.
 204 In order to use a dimensionless variable, a parameter r_N is defined:

$$r_N^{(\beta)} \equiv \frac{ECF(N+1, \beta)}{ECF(N, \beta)}. \quad (4)$$

205 The idea of r_N comes from N-subjettiness τ_N . Both r_N and τ_N are linear in the
 206 energy of the soft radiation for a system of N partons with soft radiation. In gen-
 207 eral, if the system has N subjets, $ECF(N+1, \beta)$ should be significantly smaller than
 208 $ECF(N, \beta)$. Therefore, we can use this feature to distinguish jets with different num-
 209 bers of subjets. As in Section 5.1, the ratio r_N/r_{N-1} , denoted by C_N , (double ratios
 210 of ECFs) is used to study the detector performance:

$$C_N^{(\beta)} \equiv \frac{r_N^{(\beta)}}{r_{N-1}^{(\beta)}} = \frac{ECF(N-1, \beta) ECF(N+1, \beta)}{ECF(N, \beta)^2}. \quad (5)$$

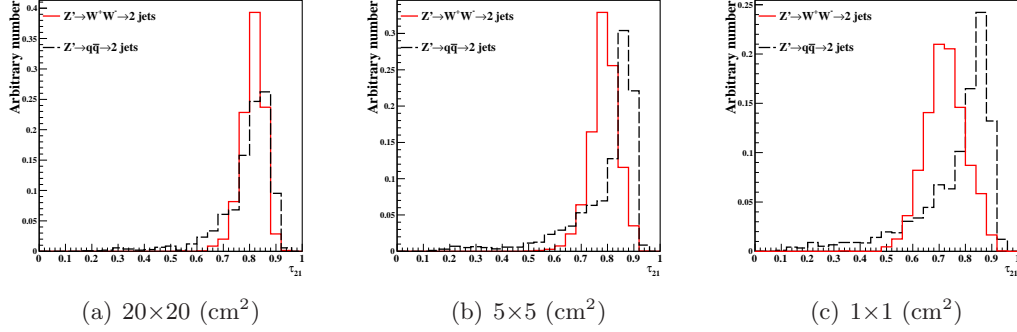


Figure 11: Distributions of τ_{21} in 20 TeV energy collision for different detector sizes. Cell sizes in 20×20 , 5×5 , and 1×1 cm^2 are shown here.

In our analysis, we set $N = 2$ and $\beta = 1$ (C_2^1).

Figure 15 presents the histograms of C_2^1 with $\sqrt{s} = 20$ TeV after making the requirement on the soft drop mass. The signal considered is $Z' \rightarrow WW$. Figure 16 shows the ROC curves from different detector cell sizes for each c.m. energy, respectively. One can see that the smallest detector cell size (1×1 cm^2) does not have the best signal/background separation power. Figure 17(c) summarizes the result of the Mann Whitney U test for C_2^1 . When c.m. energy increases, no improvement is observed from detector with the smallest cell size.

6. Conclusions

The studies presented in this paper show that the reconstruction of jet substructure variables for future particle colliders will benefit from small cell sizes of the hadronic calorimeters. This conclusion was obtained using the realistic GEANT4 simulation of calorimeter responses combined with reconstruction of calorimeter clusters used as inputs for jet reconstruction. Hadronic calorimeters that use the cell sizes of 20×20 cm^2 ($\Delta\eta \times \Delta\phi = 0.087 \times 0.087$) are least performant almost for every substructure variables considered in this analysis for jet transverse momenta between 2.5 to 10 TeV. Such cell sizes are close to those used for the ATLAS and CMS detectors at the LHC. In terms of the reconstruction of the physics-motivated quantities used for jet substructure studies, the performance of a hadronic calorimeter with $\Delta\eta \times \Delta\phi = 0.022 \times 0.022$ is, in most cases, better than for a detector with 0.087×0.087 cells. Thus this study confirms the baseline SiFCC detector geometry [7] that uses $\Delta\eta \times \Delta\phi = 0.022 \times 0.022$ HCAL cells. The performance of the HCAL with cells $\Delta\eta \times \Delta\phi = 0.0087 \times 0.0087$ and $\Delta\eta \times \Delta\phi = 0.0043 \times 0.0043$ were found to be similar.

It is interesting to note that, for very boosted jets with transverse momenta close to 20 TeV, no significant improvement with the decrease of cell sizes was observed. This result needs to be understood in terms of various type of simulations and different options for construction of the calorimeter clusters.

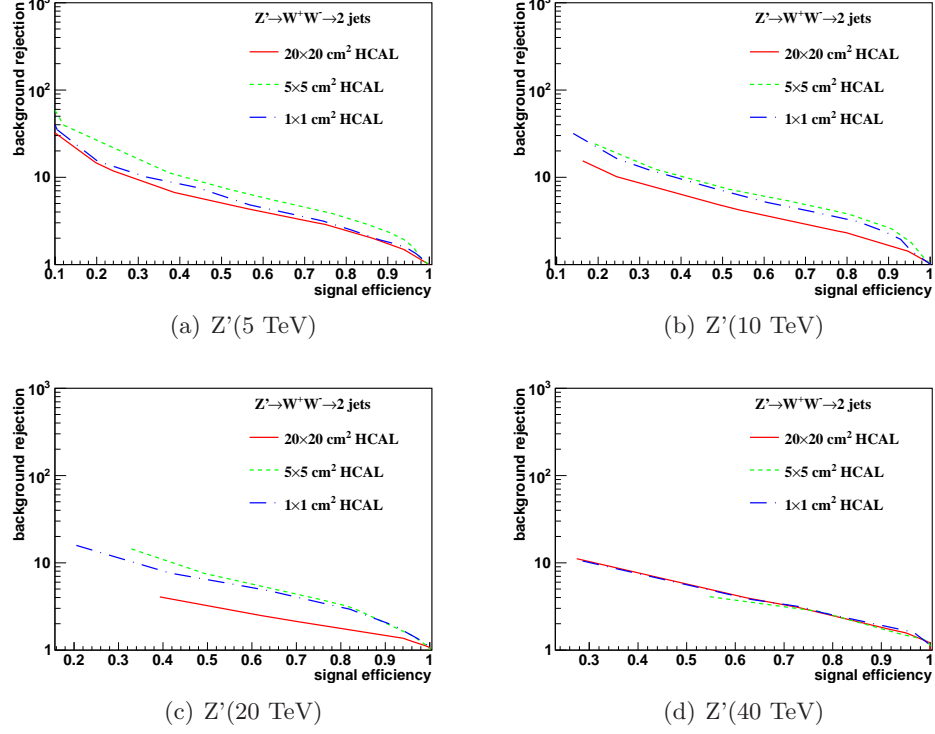


Figure 12: Signal efficiency versus background rejection rate using τ_{21} . The energies of collision at (a) 5, (b) 10, (c) 20, and (d) 40 TeV are shown here. In each figure, the three ROC curves correspond to different detector sizes.

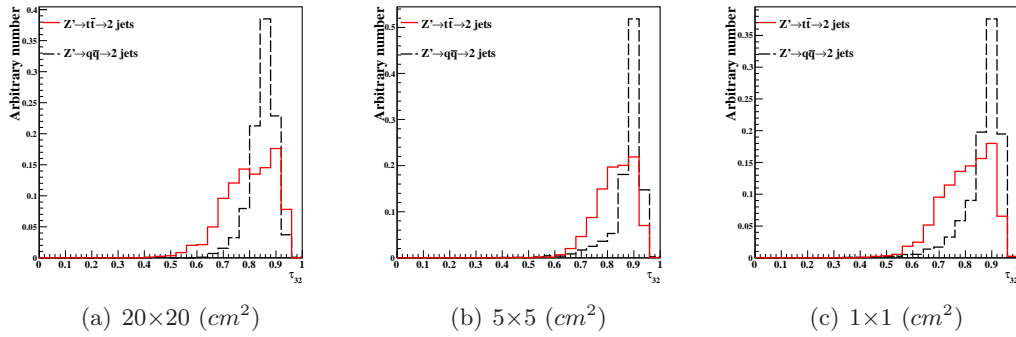


Figure 13: Distributions of τ_{32} in 20 TeV energy collision for different detector sizes. Cell sizes in 20×20 , 5×5 , and $1 \times 1 \text{ cm}^2$ are shown here.

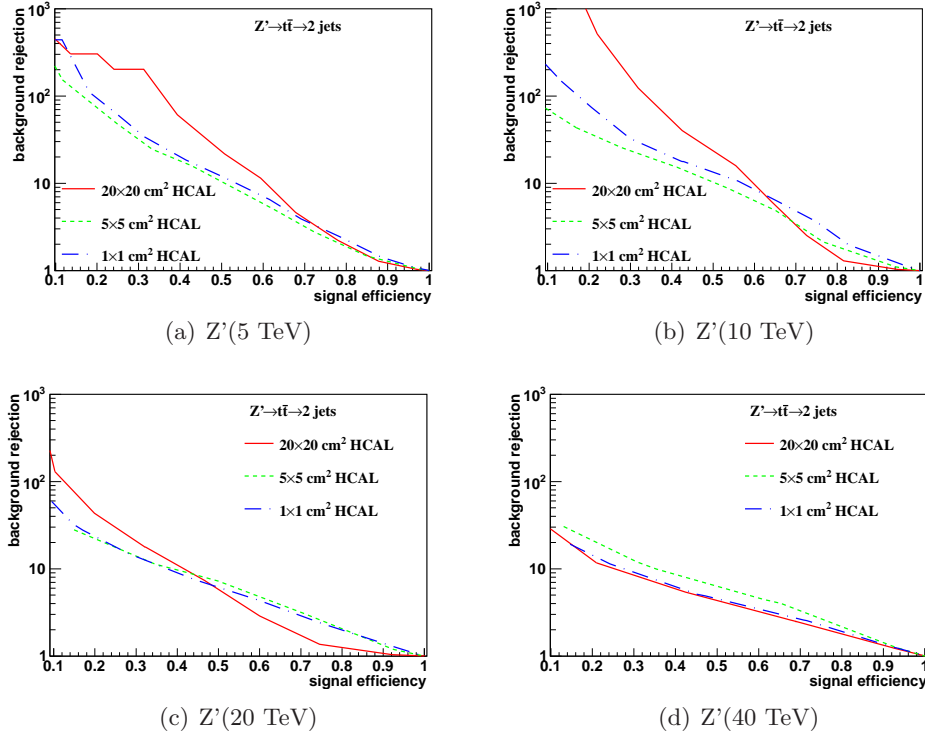


Figure 14: Signal efficiency versus background rejection rate using τ_{32} . The energies of collision at (a) 5, (b) 10, (c) 20, and (d) 40 TeV are shown here. In each figure, the three ROC curves correspond to different detector sizes.

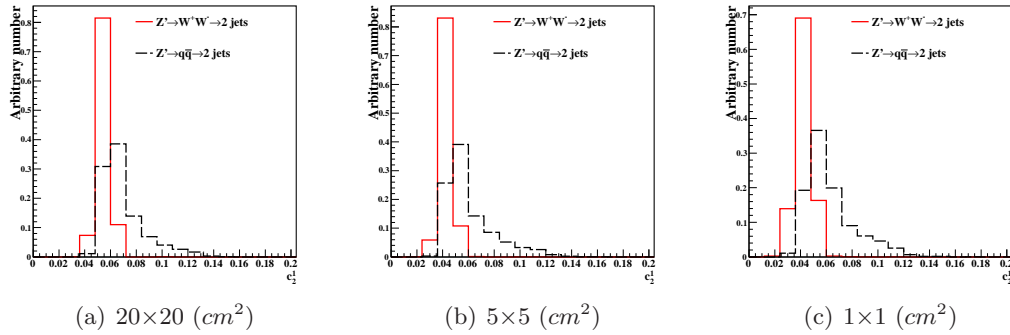


Figure 15: Distributions of C_2^1 in 20 TeV energy collision for different detector sizes. Cell sizes in 20×20 , 5×5 , and $1 \times 1 \text{ cm}^2$ are shown here.

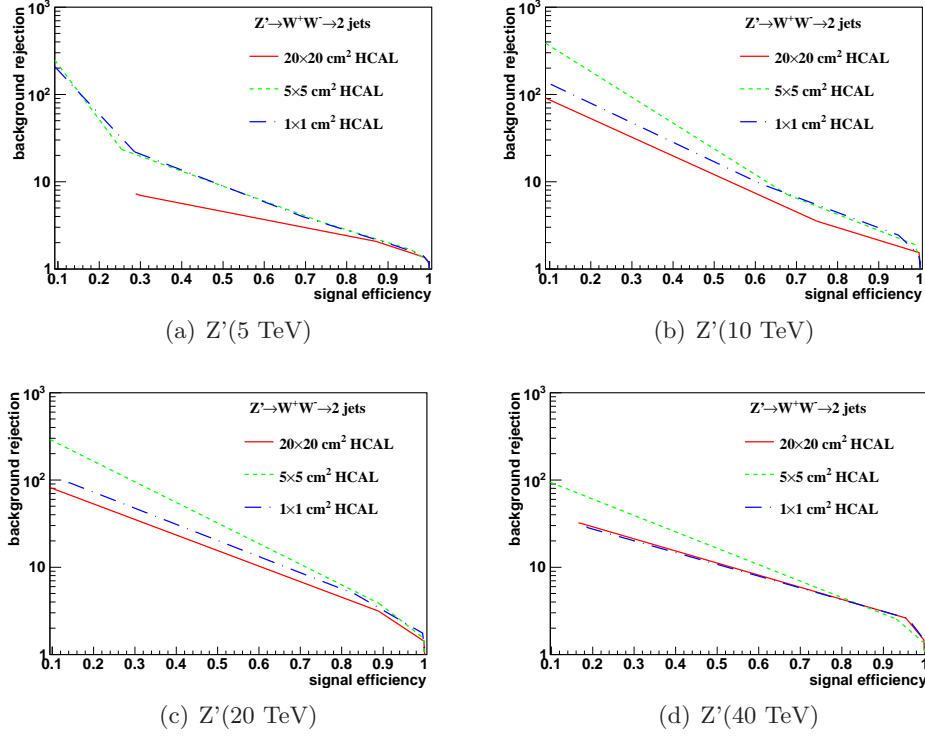


Figure 16: Signal efficiency versus background rejection rate using $C_2^{(1)}$. The energies of collision at (a) 5, (b) 10, (c) 20, and (d) 40 TeV are shown here. In each figure, the three ROC curves correspond to different detector sizes.

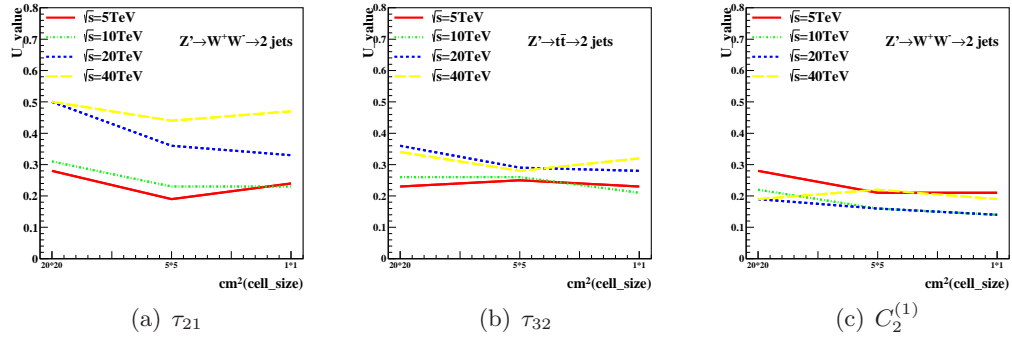


Figure 17: The Mann-Whitney U values for τ_{21} , τ_{32} , and $C_2^{(1)}$ reconstructed with different collision energies and detector cell sizes.

238 **Acknowledgements**

239 This research was performed using resources provided by the Open Science Grid,
240 which is supported by the National Science Foundation and the U.S. Department of En-
241 ergy’s Office of Science. We gratefully acknowledge the computing resources provided
242 on Blues , a high-performance computing cluster operated by the Laboratory Comput-
243 ing Resource Center at Argonne National Laboratory. Argonne National Laboratory’s
244 work was supported by the U.S. Department of Energy, Office of Science under con-
245 tract DE-AC02-06CH11357. The Fermi National Accelerator Laboratory (Fermilab) is
246 operated by Fermi Research Alliance, LLC under Contract No. DE-AC02-07CH11359
247 with the United States Department of Energy.

248 References

- 249 [1] M. Benedikt, [The Global Future Circular Colliders Effort](#) CERN-ACC-SLIDES-2016-0016. Pre-
250 sented at P5 Workshop on the Future of High Energy Physics, BNL, USA, Dec. 15-18, 2013.
251 URL <http://cds.cern.ch/record/2206376>
- 252 [2] J. Tang, et al., Concept for a Future Super Proton-Proton Collider (2015). [arXiv:1507.03224](#).
- 253 [3] R. Calkins, et al., [Reconstructing top quarks at the upgraded LHC and at future accelerators](#), in:
254 Proceedings, Community Summer Study 2013: Snowmass on the Mississippi (CSS2013): Min-
255 neapolis, MN, USA, July 29-August 6, 2013. [arXiv:1307.6908](#).
256 URL <https://inspirehep.net/record/1244676/files/arXiv:1307.6908.pdf>
- 257 [4] S. V. Chekanov, J. Dull, Energy range of hadronic calorimeter towers and cells for high-pT jets
258 at a 100 TeV collider <http://arxiv.org/abs/1511.01468> [arXiv:1511.01468](#).
- 259 [5] E. Coleman, M. Freytsis, A. Hinzmann, M. Narain, J. Thaler, N. Tran, C. Vernieri, The importance
260 of calorimetry for highly-boosted jet substructure [arXiv:1709.08705](#).
- 261 [6] DELPHES 3 Collaboration, J. de Favereau, C. Delaere, P. Demin, A. Giammanco, V. Lematre,
262 A. Mertens, M. Selvaggi, DELPHES 3, A modular framework for fast simulation of a generic
263 collider experiment, JHEP 02 (2014) 057. [arXiv:1307.6346](#), [doi:10.1007/JHEP02\(2014\)057](#).
- 264 [7] S. V. Chekanov, M. Beydler, A. V. Kotwal, L. Gray, S. Sen, N. V. Tran, S. S. Yu, J. Zuzelski, Initial
265 performance studies of a general-purpose detector for multi-TeV physics at a 100 TeV pp collider,
266 JINST 12 (06) (2017) P06009. [arXiv:1612.07291](#), [doi:10.1088/1748-0221/12/06/P06009](#).
- 267 [8] J. Allison, et al., Recent developments in Geant4, Nuclear Instruments and Methods in Physics
268 Research A 835 (2016) 186.
- 269 [9] M. J. Charles, PFA Performance for SiD, in: Linear colliders. Proceedings, International Linear
270 Collider Workshop, LCWS08, and International Linear Collider Meeting, ILC08, Chicago, USA,
271 November 16-20, 2008 , 2009. [arXiv:0901.4670](#).
- 272 [10] J. S. Marshall, M. A. Thomson, Pandora Particle Flow Algorithm, in: Proceedings, Interna-
273 tional Conference on Calorimetry for the High Energy Frontier (CHEF 2013), 2013, pp. 305–315.
274 [arXiv:1308.4537](#).
- 275 [11] G. P. S. M. Cacciari, G. Soyez, FastJet user manual CERN-PH-TH/2011-297. [arXiv:1111.6097](#).
- 276 [12] M. Cacciari, G. P. Salam, G. Soyez, The anti-kt jet clustering algorithm, JHEP 0804 (2008) 063.
277 [arXiv:0802.1189](#).
- 278 [13] S. Chekanov, HepSim: a repository with predictions for high-energy physics experiments, Advances
279 in High Energy Physics 2015 (2015) 136093, available as <http://atlaswww.hep.anl.gov/hepsim/>.
- 280 [14] B. Auerbach, S. Chekanov, J. Love, J. Proudfoot, A. Kotwal, Sensitivity to new high-mass states
281 decaying to $t\bar{t}b\bar{a}$ at a 100 TeV collider <http://arxiv.org/abs/1412.5951> [arXiv:1412.5951](#).
- 282 [15] J. Butterworth, B. Cox, J. R. Forshaw, WW scattering at the CERN LHC, Phys.Rev. D65 (2002)
283 096014. [arXiv:hep-ph/0201098](#), <http://dx.doi.org/10.1103/PhysRevD.65.096014> [doi:10.1103/](#)
284 [PhysRevD.65.096014](#).
- 285 [16] S. Catani, Y. L. Dokshitzer, M. H. Seymour, B. R. Webber,
286 [Longitudinally-invariant k-clustering algorithms for hadron-hadron collisions](#), Nuclear Physics B
287 406 (12) (1993) 187 – 224.
288 URL <http://www.sciencedirect.com/science/article/pii/055032139390166M>
- 289 [17] S. D. Ellis, D. E. Soper, Successive combination jet algorithm for hadron collisions, Phys. Rev. D48
290 (1993) 3160–3166. [arXiv:hep-ph/9305266](#), <http://dx.doi.org/10.1103/PhysRevD.48.3160> [doi:](#)
291 [10.1103/PhysRevD.48.3160](#).
- 292 [18] ATLAS Collaboration Collaboration, G. Aad, et al., Jet mass and substructure of inclusive jets in
293 $\sqrt{s} = 7$ TeV pp collisions with the ATLAS experiment, JHEP 1205 (2012) 128. [arXiv:1203.4606](#),
294 [doi:10.1007/JHEP05\(2012\)128](#).
- 295 [19] A. J. Larkoski, S. Marzani, G. Soyez, J. Thaler, Soft Drop, JHEP 05 (2014) 146. [arXiv:1402.2657](#),
296 [doi:10.1007/JHEP05\(2014\)146](#).
- 297 [20] Y. L. Dokshitzer, G. D. Leder, S. Moretti, B. R. Webber, Better jet clustering algorithms, JHEP
298 08 (1997) 001. [arXiv:hep-ph/9707323](#), <http://dx.doi.org/10.1088/1126-6708/1997/08/001> [doi:](#)
299 [10.1088/1126-6708/1997/08/001](#).
- 300 [21] M. Wobisch, T. Wengler, Hadronization corrections to jet cross-sections in deep inelastic scattering,
301 in: Monte Carlo generators for HERA physics. Proceedings, Workshop, Hamburg, Germany, 1998-
302 1999, 1998, pp. 270–279. [arXiv:hep-ph/9907280](#).

- 303 [22] J. Thaler, K. Van Tilburg, Identifying Boosted Objects with N-subjettiness, JHEP 03 (2011) 015.
304 [arXiv:1011.2268](#), [doi:10.1007/JHEP03\(2011\)015](#).
- 305 [23] S. Catani, Y. L. Dokshitzer, M. H. Seymour, B. R. Webber, Longitudinally-invariant k_{\perp} -clustering
306 algorithms for hadron-hadron collisions, Nucl. Phys. B 406 (CERN-TH-6775-93. LU-TP-93-2)
307 (1993) 187–224.
- 308 [24] F. A. Dreyer, L. Necib, G. Soyez, J. Thaler, Recursive Soft Drop, JHEP 06 (2018) 093.
309 [arXiv:1804.03657](#), [doi:10.1007/JHEP06\(2018\)093](#).
- 310 [25] A. J. Larkoski, G. P. Salam, J. Thaler, Energy Correlation Functions for Jet Substructure, JHEP
311 06 (2013) 108. [arXiv:1305.0007](#), [doi:10.1007/JHEP06\(2013\)108](#).